Towards improving the capacity of UiO-66 for antibiotic elimination from contaminated water

Sara Rojas, Ana Torres, Víctor Dato, Fabrice Salles, David Ávila, Jessica García-González, Patricia Horcajada

Towards improving the antibiotic elimination capacity of UiO-66 from contaminated water

Sara Rojas,[a,b] Ana Torres,[a] Víctor Dato,[a] Fabrice Salles,[c] David Ávila,[d] J. García-González,[e] Patricia Horcajada [a,*]

Antibiotics are found in natural waters, raising the concerns about their human and environmental toxicity and wide occurrence of antibiotic resistant bacteria. The antibiotic resistance crisis is attributed to the overuse and misuse of these medications. Particularly, sulfamethazine (SMT), an antibiotic commonly used in pigs and cattle for the treatment of bacterial diseases, has been severely detected in natural environments (soil and water). Among all the technologies developed to combat the deteriorating water quality and control antimicrobial resistance, the heterogeneous photocatalysis should be highlighted for the degradation of refractory organic compounds. Here, we described the SMT adsorption and photodegradation capacity of a highly porous and robust zirconium-based MOF UiO-66 under realistic conditions, and its potential recyclability. Futher, its SMT removal capacity was improved by nanosizing the MOF (100% of SMT degradation in only 4 h for nanoUiO-66), and funtionalizing the MOF porosity (28.5% in 24 h for nanoUiO-66-NH_2), respectively. Finally, the safety of the formed by-product during the SMT photodegradation was confirmed, reinforcing the potential of the applicaton of UiO-66 in water remediation.

Introduction

Antibiotics are essential for the maintenance of public health and life quality. Thousands of different active compounds are currently used in large quantities to treat human and livestock diseases. Concerning human maladies, only in 2018, 20.1 systemic doses of antibiotics were administered *per* 1000 inhabitants *per* day in the European Union, according to the annual report from the European Center for Disease Prevention and Control.[1] On the other hand, only in Spain, 1102 tons of veterinary antibiotics were commercialized in 2009 according to the Spanish Agency for Medicines and Health Products, 80% of them coming from four main groups of antimicrobials: 31% of tetracycline, 22% of sulfonamides and trimethoprim, 16% of *β*-lactams, and 8% lincosamides.[2] As a consequence of their extensive/intensive use, antibiotics are found in natural waters, raising the concerns about their human, animal, and environmental toxicity, and widening the occurrence of antibiotic resistant bacteria (ARB).[3–5] In this sense, due to both their significance for human and veterinary medicine and their persistence, sulfonamides, quinolones, and trimethoprim are the most detected antibiotics in water.[6] Particularly, the sulfonamide sulfamethazine (SMT), frequently used in pigs and cattle,[7,8] has been detected in natural environments such as soil or water, ranging from a few nanograms to tens of milligram *per* litre or kg of soil (from 0.6 to 20 ppm).[9–11] Because of their continuous anthropogenic introduction into the environment, aquatic organisms are chronically exposed to SMT.[12] Thus, national programs to combat the deteriorating water quality and control antimicrobial resistance are trying to reduce the indiscriminate antibiotics use, and also to develop more efficient wastewater treatment technologies. Among these last, different advanced oxidation processes have emerged as a promising way to remove antibiotics from contaminated water in the last decades.[13] These processes enable the degradation of refractory organic compounds by the *in situ* generation of reactive oxygen species (ROS; mainly hydroxyl radicals), via Fenton processes, ozonation, electrochemical oxidation, heterogeneous photocatalysis, or their combination.[14] In particular, heterogeneous photocatalysis highlights for the treatment of hazardous organic pollutants since operates at mild conditions (ambient temperature and pressure) and is considered as a green technology, its mechanism relying on the light irradiation to convert toxic pollutants to non-toxic molecules by using O_2 as main reactive.[15] Basically, the photocatalyst generates a transient state by using light absorption (photon energy) and releasing the electron-hole pair to produce the chemicals (chemical energy). The increasing attention in the use of photocatalysts for water purification has resulted in the design and development of a wide variety of photocatalysts (*i.e.,* metal oxides – TiO_2, ZnO; metal sulphides – ZnS, CdS; ternary compounds – $BaTiO_3$, Bi_2WO_6; and multicomponent materials – $BiVO_4/Bi_2OCO_3$).[16] However, these materials show some limitations in water treatment, like toxicity (*e.g.,* CdS medium oral lethal dose-LD_{50} in rats = 7080 $mg{\cdot}Kg^{-1}$), high cost, low photochemical stability (*e.g.*, metal sulphides), difficulty in recovery from water (*e.g.*, ZnO, TiO_2),[17] and/or inefficient UV-vis light absorption (*e.g.,* TiO_2 absorbs only 3% of the entire solar spectrum).[18]

In this context, a new class of crystalline porous materials, known as Metal-Organic Frameworks (MOFs), has attracted an increasing attention as photocatalysts. MOFs are comprised of inorganic nodes and polydentate organic linkers that assemble into multidimensional periodic lattices through coordination bonds, providing a robust and well-defined network and also a high porosity.[19] Compared to the previously mentioned photocatalysts, MOFs present an exceptional versatility, with a broader range of possibilities regarding the interaction between their inorganic and organic parts. In this line, the metal clusters can be regarded as inorganic semiconductor quantum entities, which are in close contact with the organic ligands, serving these lasts as antennas to activate the semiconductor quantum dots. Recently, MOFs have been proposed as heterogeneous photocatalysts in organic pollutants elimination.[20] However, most of these studies address the removal of small molecules and organic dyes, remaining the elimination of macromolecular antibiotics from contaminated water poorly investigated. Further, in the elimination of antibiotics, pure MOFs have been mainly used as adsorbents, with only 3 examples of their use as photocatalyst. Coupled with persulfate (PS-

persulfate oxidation process), MIL-88A(Fe) and MIL-101(Cr) were described as photocatalysts in the successful degradation of tetracycline hydrochloride (100% of removal in 90 min, 200 ppm, pH = 3.45) and sulfadimethoxine (97.8% of removal in 90 min at 60 ºC), respectively.[21,22] Very recently, a newly synthetized $[Zn_6(IDC)_4(OH)_2(HPRZ)_2]_n$ composed by Zn(II) cations and piperazine (HPRZ) and imidazole-4,5-dicarboxylate (IDC) ligands was used as catalyst in the photodegradation of amoxicillin (37%, 180 min).[23] However, these reports do not consider MOF stability, and use purified water (Milli-Q or deionized) or other necessary species (*i.e.,* PS) to perform the degradation process, which is far from complex river compositions or their functional application in WWTPs.

Here, we describe the SMT photodegradation capacity of a highly porous and robust benchmarked zirconium-based MOF, UiO-66 ($[Zr_6O_4(OH)_4(BDC)_{12}]$ H_2BDC = 1,4-benzenedicarboxylic acid)UiO-66 is based on Zr(IV) oxoclusters and terephthalate anions, possessing octahedral and tetrahedral cavities (~11 and ~8 Å, respectively) accessible through triangular micropores (*ca.* 5 – 7 Å).[24,25] Its very high important porosity, its essential structural stability in water, as well as its photocatalytic activity, makes UiO-66 an excellent candidate to be used in the photochemical degradation of SMT from water.

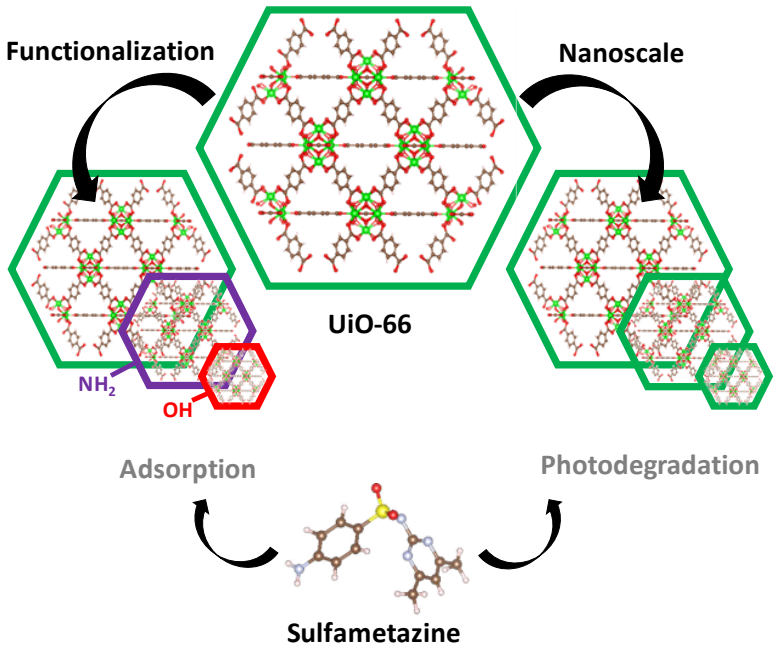

Figure 1. Schematic view of the structure of UiO-66 (zirconium polyhedra, oxygen, and carbon are represented in green, red, and grey, respectively; hydrogen atoms are omitted for clarity). Structure of the antibiotic SMT is also given (sulphur is represented in yellow).

First, we have evaluated the UiO-66 stability and SMT removal capacity (adsorption and photodegradation) in tap water. Remarkably, SMZ elimination studies were conducted under realistic conditions (*i.e.,* tap drinking water, ambient temperature, neutral pH, in absence of other additives for the treatment, etc.) considering its potential recyclability, which highlights the interest of this work. Subsequently, in a way to further improve the SMT elimination capacity, the SMT elimination was rationalized by investigating the influence of crystal size and functionalization of UiO-66, by using the series of functionalized nanosized UiO-66s (nanoUiO-66-X; X = H, NH_2, and OH). Last but not least, we have identified the formed by-products during SMT photodegradation, considering their potential toxicity, in order to assess the impact or the water treatment with UiO-66.

Results and discussion

A. Photodegradation of SMT using the robust UiO-66

To evaluate the ability of UiO-66 in water purification, the powdered material was first suspended in a tap water solution of SMT, using a concentration range within that one commonly found in wastewater (*i.e.,* 10 ppm of SMT).[9–11] UiO-66 photocatalytic activity towards the degradation of SMT was investigated under UV-visible light irradiation, quantifying the contaminant elimination by high performance liquid chromatography (HPLC). In the same manner, the SMT adsorption capacity of UiO-66 was performed under dark. In addition, UiO-66 stability was monitored during the SMT photodegradation/adsorption processes by means of the quantification of the ligand leaching by HPLC. Remarkably, UiO-66 was able to photodegrade up to 77 ± 4 % of SMT within 24 h, while proving an excellent chemical stability (only 1.6 ± 0.9% of degradation, *ca.* 0.005 ppm; **Figure 2a**) and structural robustness (as confirmed by X-ray powder diffraction; XRPD, **Supporting information, Figure S1a**). These stability analyses are fundamental when MOFs are proposed for water remediation in order to avoid an extra contamination, originated from the matrix degradation.[26] Unlike its remarkable SMT photodegradation capacity, UiO-66 can eliminate by adsorption only 3.5% of SMT within 24 h.

The excellent SMT removal (photodegradation) capacity and stability of UiO-66 prompt us to further investigate the potential recyclability of this MOF. Upon 4 cycles of the photodegradation process, UiO-66 efficiently removed SMT without a significant decrease in efficiency (**Figure 2b**). After 4 cycles, although the solid showed a significant broadening of the Bragg peaks, consistent with a loss of long range structural, chemical stability was fully kept (with no additional ligand leaching; see **Supporting information** and **Figure S2**).

In an attempt to further improve the SMT photodegradation capacity of UiO-66, we have taken advantage of MOFs' unique possibilities, and two strategies were considered*: i)* reduction of the particle size, and *ii)* tuneability of the light absorption by introduction of substituents on the aromatic linker. Regarding particle size, it is generally considered that smaller particles will favour the catalytic reactions. However, we know about the limitations of determining the particle size effects in catalyst, since MOFs' structure (*e.g.,* density of defects and degree of crystallinity of MOF) may change during the synthesis as particle size decreases.[27] Tentatively, we have considered that if the reaction occurs in the inner surface, the transport of reactants and products will be faster in small particles. On the opposite, if the reaction occurs on the outer surface, the increased specific surface area will favour the reactivity. In relation to the second strategy, the modification of nanoUiO-66 by ligand functionalization could result in an enhancement of the photoconversion quantum yield and could allow the extension of the absorption band gap to visible light, enabling water remediation under sunlight.[28] Further, the introduction of functional groups into the MOF network will affect the reactivity with SMT (*e.g.,* changing the hydrophobic/hydrophilic character of the framework, favouring the formation of hydrogen bonds, etc.). In this regard, we have modified the benzenedicarboyxlate of nanoUiO-66-X with an amine (NH_2) and hydroxyl group (OH).

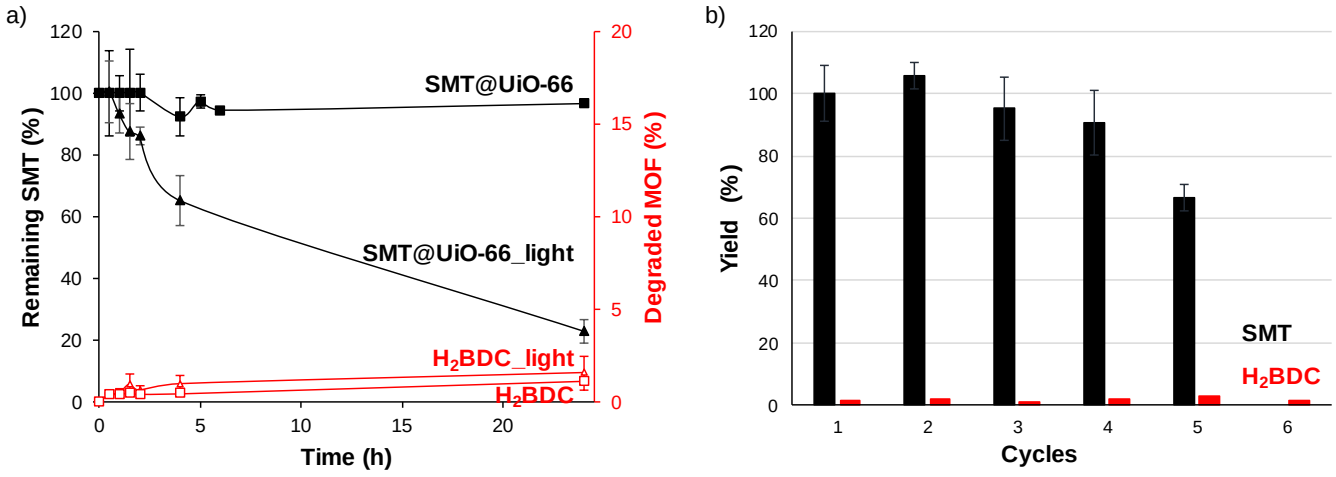

Figure 2. a) SMT photodegradation and adsorption kinetics under UV-vis irradiation (black triangles, left y axis) and darkness (black squares, left y axis) in the presence of UiO-66, respectively. The MOF degradation, by means of H_2BDC leaching, was also represented under UV-vis light (red triangles, right y axis) and dark (red squares, right y axis) conditions. b). Cyclability tests of SMT photodegradation using UiO-66.

Thus, a series of nanoUiO-66-X (X = H, NH_2, and OH) was synthetized at room temperature and ambient pressure, with some modification of the previously reported methodology.[29] The crystallinity and porosity of the nanoUiO-66-X series were confirmed using XRPD and N_2 sorption measurements at 77 K (**Supporting information, Figure S3, Table S1**). Further, the obtained series of porous polycrystalline nanoUiO-66-X were found to be smaller (81 ± 27, 38 ± 17, and 118 ± 68 nm; for X = H, NH_2, and OH, respectively) than the initial UiO-66 material (672 ± 181 nm, **Supporting information, Figure S4**). The colloidal stability of the as-prepared materials was studied under the working conditions (water at room temperature). As expected, the colloidal stability was strongly affected by the functionalization of the organic linker. DLS measurements in water of nanoUiO-66-X showed larger particles sizes, reaching 460 ± 30, 162 ± 4, and 673 ± 142 nm for X = H, NH_2, and OH, respectively (see **Supporting information, Table S2**). Considering its higher porosity (Brunauer–Emmett–Teller (BET) surface = 1130 $m^2 \cdot g^{-1}$) and water colloidal stability, one could expect that the best material to be used in the SMT elimination is the nanoUiO-66-NH_2 derivative.

To evaluate the potential application of the nanoUiO-66-X series in SMT removal from water, we studied their use in both processes (adsorption and photodegradation) following the same procedure as for UiO-66. When the matrixes were suspended in SMT tap aqueous solution in absence of irradiation, the crystalline structure of the nanoUiO-66 was kept intact, while there is an important crystallinity loss for nanoUiO-66-NH_2 and nanoUiO-66-OH derivatives (as confirmed by XRPD; **Supporting information, Figure S6**). SMT was successfully incorporated in the functionalized nanoUiO-66-NH_2 and nanoUiO-66-OH, with a 28 ± 1 and 6 ± 2 % removal capacity after 24 h, respectively (**Figure 3; Supporting information, Figure S5)**. Although the pore size dimension of UiO-66 (*ca.* 5 – 7 Å) are big enough to adsorb SMT (11 x 5 x 5 $Å^3$, estimated by Vesta considering Van der Waal radii), no SMT elimination by adsorption was achieved when using the non-functionalized nanoUiO-66. These results agree with the results obtained previously for the microUiO-66, being able to absorb only 3.5% of SMT in 24 h. In addition, the solids showed an excellent stability since only ~1% of the total H_2BDC-X ligand was leached after 24 h contact (1.4 ± 0.0%, 0.0 ± 0.0%, and 0.0 ± 0.0% for X = H, NH_2 and OH, respectively).

The adsorption of SMT on nanoUiO-66-X (X = NH_2 and OH) may be controlled by a sum of weak intermolecular forces, such as hydrophobic effect, electrostatic attraction, π-π electron donor-acceptor, and hydrogen bond interactions.[30 31] We will try to discuss the impact of each of them here. Hydrophobic/hydrophilic balance makes a critical difference during the adsorption process. We can assume that the hydrophobic/hydrophilic interactions are the only force in adsorption process at first. The adsorption can be judged by the *n*-octanol-water partition coefficient (K_{ow}) of SMT (log K_{ow} = 0.14), indicating that SMT is an hydrophilic molecule. Therefore, SMT will preferentially be adsorbed in the more hydrophilic UiO-66-NH_2 and –OH derivatives. Aside from the hydrophobic/hydrophilic balance, the nature of the nanoparticles surface will determine the interaction with the different components of the contaminated water (water molecules, ions, SMT, etc.). In this respect, considering the pK_a of SMT (pk_{a1} = 2.65 – aromatic amine; pK_{a2} = 7.65 – sulfonamide), SMT is predominantly neutral in tap water (pH = 6). Interestingly, the functionalization

of nanoUiO-66-X is a determining factor on surface charge (-17 ±1, -22 ± 1, and +23 ± 3 mV for nanoUiO-66, nanoUiO-66-OH, and nanoUiO-66-NH_2, respectively). Therefore, considering that SMT is eliminated from water when using both negatively (nanoUiO-66-OH) and positively (nanoUiO-66-NH_2) charged MOFs, the intermolecular electrostatic attraction between SMT and nanoUiO-66-X should not be the driving force of the adsorption processes. Regarding the electrostatic interactions, SMT has the electron donor –NH_2 group (named as -NH_{2_SMT}), which can interact with the benzene ring of nanoUiO-66 ligand in the π-π electron donor-acceptor interaction. Further, the π-π stacking should also be present between the benzene rings in SMT and organic ligand of nanoUiO-66-X. Again, considering that no SMT adsorption is achieved in the nanoUiO-66 material, we can claim that π-π interactions are not a predominant differential aspect in the SMT adsorption process. Finally, we have considered the hydrogen bonding, as it is regarded as an important mechanism to explain the adsorption of polar organics on functionalized MOFs.[32] The Fourier transform infrared (FTIR) spectra of the SMT-loaded nanoUiO-66-X (X = H, NH_2, and OH) confirmed a bands shift associated to the carboxylate group found in the range of 1520-1650 cm^{-1} and 1280 to 1400 cm^{-1} for the γ_{asym} and γ_{sym} vibration bands in all the SMT loaded materials, supporting host-guest interaction by hydrogen bonding. In this regard, there is a shift from 1582 to 1578 cm^{-1} and 1395 to 1390 cm^{-1} for UiO-66-H, 1571 to 1563 cm^{-1} and 1384 to 1381 cm^{-1} for UiO-66-NH_2, and 1582 to 1570 and 1415 to 1421 cm^{-1} for UiO-66-OH, respectively. Further, some of us have recently evidenced by Monte Carlo simulations that the NH_2 or –SO_2 groups from SMT can interact with the carboxylate groups of different MOFs.

On the other hand, in order to investigate the location and conformation of the SMT molecules in the pores of the nanoMOFs and try to explain the experimental results (to define the main interactions between the solid and the SMT molecules), Grand Canonical Monte Carlo (GCMC) simulations were performed by fixing the equilibrium saturation pressure of SMT molecules at a large value, which has already proved to be an efficient way to obtain the saturation description.[33,34] In this case, calculations failed to reproduce the saturation and results show no adsorption. Two explanations can be given to explain this failure: *i)* the force-fields considered to investigate the interactions between the solids and the SMT molecules are not consistent, *ii)* or the flexibility of the framework must be taken into account. To go further, both DFT calculations (which are not dependent of any force-field) and Monte Carlo simulations (where the loadings are fixed and impose the SMT molecules to be adsorbed, see **Supporting information, Section 3**) were performed. Snapshots obtained from these new calculations in Monte Carlo are given in **Figure S8**, while the extractions of the DFT calculations are disclosed in **Figure S9**. The comparison shows a general good agreement between the main interactions elucidated from these two techniques. The force field used in classical MC simulations was consistent, and therefore the flexibility of the framework should be considered for GCMC to reproduce adsorption of large molecules. Anyway, the comparison between the main interactions clearly evidenced a different behaviour between pristine UiO-66 and the functionalized UiO-66-X (X=NH_2 or OH), in agreement with the experimental results. Indeed, considering **Figures S8a & S9a,b**, weak interactions between the $NH_{2\text{-}SMT}$ groups within the UiO-66 framework can be found (distances larger than 3.1 Å to 3.645 Å were found), and only stronger π-stacking interactions were observed (distances ranging from 3.031 to 3.364 Å, and from 3.472 to 3.844 Å from MC and DFT calculations, respectively). Furthermore, no real difference was observed between the two types of pores regarding the interaction distances. In contrast, stronger interactions were found for UiO-66-X (X= NH_2, OH),

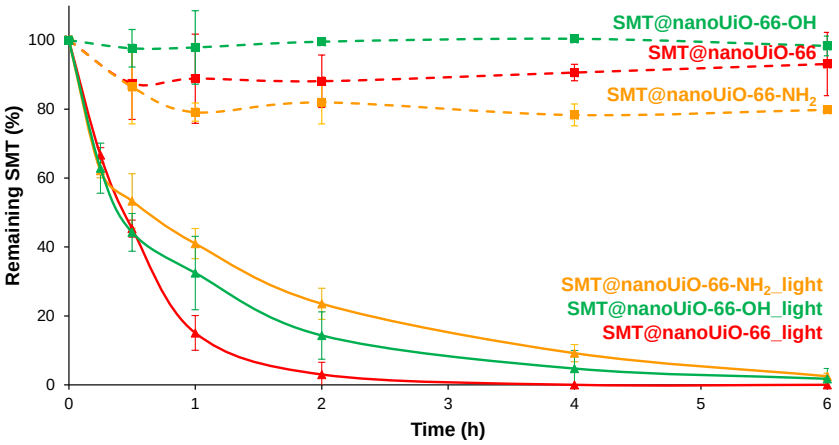

Figure 3. SMT photodegradation kinetics under dark (dashed line, squares) and UV-visible light irradiation (continuous line, triangles) in the presence of nanoUiO-66-X (X = H, NH_2, and OH) (red, yellow, and green, respectively). For clarity, the data corresponding to MOFs degradation have been here omitted (although included in Supporting information, Section 3).

where NH_{2_SMT} interacts with the NH_2 of nanoUiO-66-NH_2 with distances ranging from 2.5 to 2.992 Å (from MC simulations, **Figure S8b**), or 2.316 to 2.982 Å (from DFT calculations, **Figure S9c,d**) or NH_{2_SMT} interacts with the OH of nanoUiO-66-OH (distances close to 2 Å from both simulations **Figures S8c & S9e,f**). In these structures, a strong π-stacking was again observed with distances ranging from 3.1 to 3.6 Å in **Figures S8 & S9**). It can be noted that the larger pore seems to be the most preferential site due to the stronger interactions observed by DFT calculations. All these differences support the absence of SMT adsorption from experimental data for pristine UiO-66 (in which a weak affinity for SMT can be detected), while UiO-66-X (X=NH_2, OH) can adsorb a larger SMT amount. Considering the experimental and computational results, the adsorption of SMT in UiO-66-X (X = NH_2 and OH) may be mainly governed by hydrophobic/hydrophilic and hydrogen bond interactions. However, the comparison between the interaction distances is not sufficient to explain the different adsorption behaviour between UiO-66-OH and UiO-66-NH_2, considering the similar strong interactions between linker and SMT, or π-stacking observed in both cases. Further, a different affinity for the solvent could also be invoked, and SMT and solvent adsorptions could therefore be in competition.

Regarding the SMT photodegradation capacity, nanoUiO-66-X series (H = H, NH_2, and OH) was remarkably able to degrade up to 100 ± 0, 90 ± 2, and 95 ± 5% of SMT in 4 h, while keeping its chemical integrity (**Figure 3**), 0.0 ± 0.0%, 0.1 ± 0.0%, and 0.0 ± 0.0% degradation for H = H, NH_2, and OH, respectively, **Supporting information, Figure S5**). In view of these results, we can confirm that the modification of the band gap by linker functionalization does not improve the SMT photodegradation capacity of nanoUiO-66 (Eg = 3.89 eV for UiO-66 *vs.* 2.87 eV and 3.29 eV for nanoUiO-66-NH_2 and nanoUiO-66-OH, respectively; values obtained from the Tauc Plot, **Supporting information, Figure S11**).[35] Considering that the nanoUiO-66 was not able to adsorb SMT, one could conclude that the photodegradation process is not dependent on the MOF adsorption capacity, and may preferentially occur on the surface of the nanoparticle. The external surface was found to be similar for all the nanoparticles, ranging from the 387 and 386 $m^2 \cdot g^{-1}$ for the nanoUiO-66 and nanoUiO-66-NH_2, respectively, to 208 $m^2 \cdot g^{-1}$ for the nanoUiO-66-OH. On the other side, the XRDP results showed that only nanoUiO-66 keeps intact its crystalline structure, while nanoUiO-66-NH_2 and nanoUiO-66-OH suffer an important amorphization (**Supporting information, Figure S6**). In an attempt to rationalize these results, we could conclude that the lower activity found with NH_2 and OH functionalities should be attributed to both the electronic structure modulation that negatively affects the activity of the exposed Zr ions and the amorphization of the nanoUiO-66-NH_2 and nanoUiO-66-OH frameworks.[36]
In order to compare the SMT degradation kinetics and to gain further understanding on the involved mechanism, the SMT degradation kinetics using all nanoUiO-66-X materials were fitted to a first order kinetics according to Eqn (1) (**Supporting information, Figure S12**). The best SMT degradation rate is obtained when using the nanoUiO-66. The fitting of the data gives rise to a *k* value of 1.7835 h^{-1}, *ca.* 20 times higher than the UiO-66, and 2.7 and 2 times higher than the nanoUiO-66-NH_2 and nanoUiO-66-OH, respectively (**Supporting information, Table S3**). Finally, to contextualize these results, nanoUiO-66 provided a fast SMT photodegradation than the micrometric UiO-66 (100 ± 0 *vs.* 35 ± 8% in 4 h, respectively), evidencing the relevance of the higher external surface area of nanoUiO-66 *vs*. UiO-66 (287 *vs.* 192 $m^2 \cdot g^{-1}$, respectively). This removal efficiency can be compared with other proposed systems in SMT elimination (**Supporting information, Table S3**). Considering both, the adsorption and photocatalytic studies, these fittings also reveal that the rate-limiting step of the photodegradation is not the physisorption of the SMT on the MOF microporosity, but the photocatalytic reaction on the Zr-O active sites, after MOF photon absorption by the ligand-to-cluster transfer mechanism. In view of these results, one could argue that the functionalization of the pore mainly impacts the adsorption process, while the particle size of the MOF affects the photocatalysis in SMT elimination from water.

$$Ln[SMT] = -Kt + Ln[SMT]_0 \qquad \text{Eqn (1)}$$

The hazard of antibiotics in the environment does not only depend on their concentration but also their metabolites or degradation products, which can sometimes be more harmful than the parent compound.[37] Previous studies have described the photochemical behaviour of sulfonamides, determining that degradation occurs through cleavage at various positions.[38,39] The identification of the photodegradation products of SMT formed after 24 h-irradiation of the SMT + UiO-66 system in aqueous medium (pH = 6) was performed based on the results of ultra-high performance liquid chromatography coupled to mass spectroscopy (UHPLC/MS), supported with fragmentation patterns obtained from MS/MS experiments. Initially, the fragmentation pattern of SMT gave us the information needed to deduce several substituents and identify the unknown intermediates (**Supporting information, Figure S13**). Although the determination of the SMT degradation pathway is out of the scope of this work, we have identified some intermediates deduced from their estimated molecular weight to assess the potential toxicity of the resulting products. The fragment ion *m/z* 215 (*N*-(4,6-dimethylpyrimidin-2-yl)benzene-1,4-diamine) was attributed to the product from SO_2 extrusion, a phenomenon frequently shown in sulfonamides.[40] Further, an attack of a hydroxyl radical at the carbon-nitrogen bond of the benzene ring might result in the fragment derived from the pyrimidinyl portion (*m/z* 124), leading to the formation of the 2-amino-4,6-dimethoxypyrimidine product. It should be pointed that the formation of the 2-amino-4,6-dimethoxypyrimidine as SMT photodegradation intermediate was also quantified by HPLC (3.6% after 24 h). Regarding the potential toxicity of the degradation products, although all molecules (*N*-(4,6-dimethylpyrimidin-2-yl)benzene-1,4-diamine; 2-amino-4,6-dimetoxypyrimidine and SMT) are classified as irritant (according to the Globally Harmonized System of Classification and Labelling of Chemicals-GHS), only SMT is described as health hazard, with a medium lethal dose (LD_{50}, oral, mouse) of 50 $g \cdot kg^{-1}$.[41] Notably, these results suggest that when using UiO-66 as photocatalyst, we are generating degradation products with lower toxicity than SMT, improving the quality of water.

C Conclusions

In this work, we present the successful utilization of the Zr-based MOF UiO-66 in the elimination of the emerging contaminant SMT. Its ability to remove (by photodegradation and adsorption) this challenging antibiotic can be improved by nanosizing the MOF (from 77 to 100% by photocatalysis) and functionalizing its porosity (from 0 to 28% by adsorption), respectively. The functionalization of the pore mainly impacts on the adsorption process controlled by hydrophobic/hydrophilic and hydrogen bond interactions, while the particle size and the stability of the MOF affects the photocatalysis in SMT elimination from water. Upon photodegradation of the antibiotic SMT, by using UiO-66 as photocatalyst we are generating products with lower potential toxicity than SMT, improving the quality water.

Materials and methods

All reactants were commercially obtained from Sigma–Aldrich (sulfamethazine (SMT, ≥99%), zirconium(IV) propoxide solution (70 wt.% in 1-propanol), zirconium (IV) chloride ($ZrCl_4$, ≥99%), terephthalic acid (H_2BDC, ≥98%), 2-hydroxyterephthalic acid (H_2BDC-OH,

≥97%), 2-amino-4,6-dimethoxypyrimidine), Acros Organics (2-aminoterephtalic acid (H_2BDC-NH_2, 99%), Chemlab (*N*,*N*-dimethylformamide (DMF, 99.5%)), and Labkem (methanol (MeOH)), and used without further purification.

Physicochemical characterization. Fourier transform infrared (FTIR) spectroscopic analyses were performed in a Nicolet 6700 (Thermo Scientific, USA) infrared spectrometer with the help of an attenuated total reflectance (ATR) diamond accessory. Nitrogen isotherms were obtained at 77 K using an AutosorbQ2 (Quantachrome Instruments, USA). Before the measurement, samples were evacuated at 200 °C overnight (on) under vacuum for UiO-66, and first at 80 ºC on and then at 150 ºC on under vacuum for all the nanoUiO-66 MOFs. Specific surface area was determined by applying Brunauer, Emmett & Teller equation (BET) in the relative pressure interval p/p_0 = 0.01-0.3 (being p_0 the saturation pressure). Pore volume and pore size distribution were calculated by the non-localized density functional theory (NLDFT) and the Horvath-Kawazoe (HK) methods, respectively. Routine X-ray powder diffraction (XRPD) patterns were collected using a conventional PANalytical Empyrean powder diffractometer (PANalytical Lelyweg, Netherlands, ϑ-2ϑ) using λCu $K_{\alpha1}$, and $K_{\alpha2}$ radiation (λ = 1.54051 and 1.54433 Å). The X-ray powder diffraction (XRPD) patterns were carried out with a 2ϑ scan between 3-35° and 3-90° with a step size of 0.013° and a scanning speed of 0.1°·s^{-1}. Thermogravimetric analyses (TGA) were carried out in an SDT Q-600 thermobalance (TA Instruments, New Castle, DE, USA) with a general heating profile from 30 to 600 °C with a heating rate of 5 °C·min^{-1} under air using a flux of 100 mL min^{-1}. Scan and transmission electron microscopy (SEM and TEM) images were taken with a Hitachi TM1000, and a Technai 20 TEM microscope (Philips, Amsterdam, the Netherlands) with a 200 kV acceleration voltage, respectively. For sample preparation, 1 mg of sample was dispersed in 10 mL of ethanol and sonicated with an ultrasound tip (UP400S, Hilscher, Teltow, Germany) for 30 sec. For observation, 1 µL of the prepared solution was dropped over a copper TEM support with a carbon mesh (lacey carbon, 300 mesh, copper, approx. grid hole size: 63 µm, TED PELLA Redding, California, USA). Particle size was monitored via counting with ImageJ software.[42] The mean particle size was statistically estimated (n > 200). The particle size and ζ-potential determinations were performed using a Malvern Nano-ZS, Zetasizer Nano Series. *Ca.* 1 mg of nanoUiO-X was dispersed in 10 mL of tap water using an ultrasound tip (Digital Sonifer 450, Branson; 10% of amplitude and for 1 min). UV-visible spectroscopic analysis of UiO-66-OH was run in a Perkin Elmer® Lambda 1050 UV/vis/NIR (Perkin Elmer, Waltham, MA, USA). The photoirradiated solutions were analyzed using a Shimadzu LCMS8030 accurate mass quadrupole coupled to ultra-high performance liquid chromatography (UHPLC) in the facilities of the Complutense University of Madrid using the same conditions as for the HPLC analysis (see below).

Different organic molecules were analyzed by HPLC: the amount of degraded SMT, as well as the released corresponding linkers (H_2BDC, H_2BDC-NH_2, or H_2BDC-OH), and the degradation product 2-amino-4,6-dimethoxypyrimidine were determined using a reversed phase HPLC Jasco LC-4000 series system, equipped with a PDA detector MD-4015 and a multisampler AS-4150 controlled by ChromNav software (Jasco Inc, Japan). A Purple ODS reverse-phase column (5 µm, 4.6 x 150 mm, Análisis Vínicos, Spain) was employed. For the quantification of all chemical species, isocratic conditions were used. The flow rate was 1 mL·min^{-1}, and the column temperature was fixed at 298 K. In all cases, the injection volume was 30 µL. The mobile phase was based on a mixture of 50:50 MeOH:phosphate buffered solution (PBS; 0.04 M, pH = 2.5) for H_2BDC, H_2BDC-NH_2, and H_2BDC-OH ligands analysis, with a retention time (rt) and an absorption maximum of 3.6 min and 202 nm, 2.8 min and 225 nm, and 2.6 min and 209 nm, respectively. SMT was analyzed using a mixture of 35:65 acetonitrile:water, with a rt of 2.7 min and an absorption maximum of 263 nm. 2-amino-4,6-dimetoxipirimidine was analyzed using a mixture of 50: 50 MeOH:H_2O with a rt of 4.3 min and an absorption maximum of 288 nm.

Preparation of the phosphate buffered solution (0.04 M, pH = 2.5): 0.02 mol (2.4 g) of NaH_2PO_4 and 0.02 mol (2.84 g) of Na_2HPO_4 were dissolved in 1 L of Milli-Q water. The pH was then adjusted to 2.5 with H_3PO_4 (≥85%) and to basic pH with NaOH 10 M.

Synthesis of UiO-66 and nanoUiO-66-X (X = H, NH_2, and OH)

UiO-66 or [$Zr_6O_4(OH)(C_8H_4O_4)_6$] nH_2O.[25] 1 mmol of $ZrCl_4$ (233 mg) and 1 mmol of H_2BDC (166 mg) were dispersed in 3 mL of DMF, placed in a teflon-lined autoclave and heated for 12 h at 200 °C. The resulting solid was recovered by filtration and washed with deionized water and acetone. 200 mg of the solid were suspended in 100 mL of DMF under stirring for 12 h. Then, the DMF-washed solid was suspended in 100 mL of MeOH under stirring for 12 h, recovering the activated solid by filtration.

nanoUiO-66-X (X = H, NH_2, and OH).[29] A mixture of 142 µL of a 70 wt.% zirconium propoxide [$Zr(OnPr)_4$] solution in 1-propanol (52 mg, 0.316 mmol), 14 mL of DMF, and 8 mL of acetic acid (140 mmol) was heated at 130 °C for 2 h under stirring. Then the solution was allowed to cool to room temperature (RT). Finally, the desired linker (149 mg, 0.90 mmol of H_2BDC; 163 mg, 0.90 mmol of H_2BDC-NH_2; or 42 mg, 0.23 mmol of H_2BDC-OH) was added, and the obtained solution was briefly sonicated for 30 s and allowed to stir at 200 rpm for 18 h at RT. Then the nanoMOF was separated from the supernatant by centrifugation (5 min, 13000 rpm) and was washed 3 times with DMF (10 mL) and 1 time with acetone (10 mL). Samples were heated at 80 °C in a vacuum oven overnight before being analyzed.

Adsorption and/or photocatalytic degradation of SMT from water using UiO-66 or nanoUiO-66-X (X = H, NH_2, and OH) series

The adsorption/photocatalytic activity of UiO-66 and nanoUiO-66-X was evaluated in terms of elimination of the emerging organic contaminant SMT as challenging antibiotic in water. In a typical experiment, 4 mg of UiO-66 or nanoUiO-66-X (X = H, NH_2, and OH) were suspended in 4 mL of a SMT tap-aqueous solution (10 ppm, according with the concentration of SMT found in the environment).[9] Adsorption/photodegradation reactions were performed under stirring. At certain intervals (0.25, 0.5, 1, 2, 4, 6, and 24 h), an aliquot of 100 µL was collected by centrifugation for HPLC analysis (SMT and the corresponding ligand). All experiments were performed at least in triplicate to ensure statistically reliable results. The crystallinity of all the remaining solids was analyzed by XRPD. First of all, the stability of an aqueous solution of SMT was studied under UV-vis light. It was verified that SMT was not degraded (after 24 h) under UV-vis light irradiation.

SMT photodegradation products: Particularly in the photodegradation studies, after 24 h of UV-vis irradiation, an aliquot was analyzed by mass quadrupole coupled to UHPLC to determine the final products of the photodegradation. A standard sample of SMT was measured to deduce through comparison the mass parents obtained.

The photodegradation experiments were performed in a photoreactor equipped with a 300 W Xe lamp (Oriel Instrument OPS-A500) under open air at RT, with the samples stirred and placed at a fixed distance of 21 cm from the irradiation source. It has to be pointed that prior to irradiation it is not necessary to stir the suspension until the adsorption-desorption equilibrium is reached. Although all the nanoUiO-66-X (X = H, NH_2, and OH) materials show a different experimental band gap (3.89, 2.87 eV, and 3.29 eV for UiO-66, UiO-66-NH_2, and UiO-66-OH, respectively; values obtained by the Tauc Plot),[35] we have irradiated all samples under all the UV-vis spectra.

Photodegradation kinetics: To shed some light on the SMT degradation kinetics and to gain further understanding on the involved mechanism, the first 2 h of SMT degradation were fitted to a first order kinetics according to Eqn (1), where *[SMT]* and $[SMT]_0$ is the remaining concentration of SMT ($mg \cdot L^{-1}$) at the time *t* (min) and the initial SMT concentration, respectively, and *k* is the first order kinetic constant (h^{-1}).

Recyclability of UiO-66: The recyclability of UiO-66 was studied following the same procedure as previously described. 4 mg of UiO-66 were suspended in 4 mL of a SMT tap-aqueous solution (10 ppm) under UV-vis light irradiation. After 24h, the sample was centrifuged, an aliquot of 100 µL was collected for HPLC analysis (SMT and H_2BDC quantification), and the solid was suspended again in a fresh SMT aqueous solution (10 ppm) for 24 h. This process was repeated for 6 cycles.

Monte Carlo simulations

Classical Grand Canonical Monte Carlo (GCMC) calculations using SORPTION (Materials Studio 2020) were performed to extract the distribution of SMT molecules inside the pores of the different UiO-66-X (X=H, NH_2, OH) structures.[43] For that purpose, a high pressure (10^4 kPa) and the temperature (T = 300 K) were fixed. Such a procedure has already been successfully used by some of us to determine the arrangement of drug and dye molecules.[44–46] Addition calculations, where the loading is fixed at 1, 2, 3 and 4 molecules per unit cell structure were also performed. Typically, 100 x 10^6 Monte Carlo steps for equilibration and 5 x 10^6 steps for production were used to reach the equilibrium. Regarding the calculations, the Ewald summation were computed to evaluate the electrostatic contribution, while atom-atom interactions at short range (cut-off fixed at 12.5 Å) were considered for the van der Waals part. In these calculations, no flexible force field was used for the solids and structures were therefore considered as rigid. Multi-cell structures were considered in concordance with the use of the cut-off.

Before Monte Carlo simulations, the partial charges used for the solids were calculated by the QEq methodology developed by Materials Studio.[47] For the SMT, DFT calculations were performed to calculate partial charges (see **Supporting information, Figure S7**) after geometry optimization of the molecule structure using the PW91 GGA density functional and the double numerical basis set containing polarization functions on hydrogen atoms (DNP) as implemented in DMol[3] code**.** Lennard Jones parameters were taken from UFF and mixed according the Lorentz-Berthelot rules.[48]

DFT calculations

After Monte Carlo simulations, DFT calculations have been performed for UiO-66-X structures containing 2 and 3 SMT molecules (generally 1 molecule in the largest octahedral pore and 1 or 2 in the smaller tetrahedral pore). From these structures, a geometry optimization was performed to investigate the main interaction sites existing in the UiO-66-X structures and SMT molecules as a function of the pore nature. Again, DFT calculations were performed to obtain the final structure after geometry optimization using the PW91 GGA density functional and the double numerical basis set containing polarization functions on hydrogen atoms (DNP) as implemented in DMol[3] code**.**

Conflicts of interest

There are no conflicts to declare.

Acknowledgements

The work has been supported by IMDEA Energy Foundation and MOFSEIDON project (PID2019-104228RB-100, MCI/AEI/FEDER, UE). SR and P.H. acknowledges the financial support of Madrid Community (Recruitment of Young doctors 2017, Talento Modality 2, 2017-T2-IND-5149). PH acknowledges the Spanish Ramón y Cajal Programme (Gran Agreements 2104-15039). S.R. acknowledges the Spanish Juan de la Cierva Incorporación Fellowship (grant agreement no. IJC2019-038894-I).

Notes and references

1 https://www.ecdc.europa.eu/en/publications-data/surveillance-antimicrobial-consumption-europe-2018.
2 Ministerio de Sanidad Política Social e Igualdad, *Sales of veterinary antimicrobial agents in Spain in 2009*, 2011.
3 C. Ding and J. He, *Appl. Microbiol. Biotechnol.*, 2010, **87**, 925–941.
4 J. L. Martínez, *Science (80-.).*, 2008, **321**, 365–367.
5 C. Stoll, J. P. S. Sidhu, A. Tiehm and S. Toze, *Environ. Sci. Technol.*, 2012, **46**, 9716–9726.
6 I. T. Carvalho and L. Santos, *Environ. Int.*, 2016, **94**, 736–757.
7 M. Vila-Costa, R. Gioia, J. Aceña, S. Pérez, E. O. Casamayor and J. Dachs, *Water Res.*, 2017, **115**, 309–317.

8 K. Hruska and M. Franek, *Vet. Med. (Praha).*, 2012, **57**, 1–35.
9 M. Petrovic and P. Verlicchi, *Contrib. to Sci.*, 2014, **10**, 135–150.
10 D. J. Lapworth, N. Baran, M. E. Stuart and R. S. Ward, *Environ. Pollut.*, 2012, **163**, 287–303.
11 S. Managaki, A. Murata, H. Takada, C. T. Bui and N. H. Chiem, *Environ. Sci. Technol.*, 2007, **41**, 8004–8010.
12 P. Grenni, V. Ancona and A. Barra Caracciolo, *Microchem. J.*, 2018, **136**, 25–39.
13 R. Yin, W. Guo, H. Wang, J. Du, X. Zhou, Q. Wu, H. Zheng, J. Chang and N. Ren, *Chem. Eng. J.*, 2018, **334**, 2539–2546.
14 A. R. Ribeiro, O. C. Nunes, M. F. R. Pereira and A. M. T. Silva, *Environ. Int.*, 2015, **75**, 33–51.
15 D. Ravelli, D. Dondi, M. Fagnoni and A. Albini, *Chem. Soc. Rev.*, 2009, **38**, 1999–2011.
16 J. Bedia, V. Muelas-Ramos, M. Peñas-Garzón, A. Gómez-Avilés, J. J. Rodríguez and C. Belver, *Catalysts*, 2019, **9**, 52–95.
17 D. F. Hernández-Barreto, J. P. Rodriguez-Estupiñán, J. C. Moreno-Piraján, R. S. Ramírez and L. Giraldo, *Catalysts*, 2020, **10**, 574.
18 M. Pawar, S. T. Sendoğdular and P. Gouma, *J. Nanomater.*, 2018, **2018**, 1–13.
19 H. Li, M. Eddaoudi, M. O'Keeffe and O. M. Yaghi, *Nature*, 1999, **402**, 276–279.
20 F. X. Llabrés i Xamena, A. Corma and H. Garcia, *J. Phys. Chem. C*, 2007, **111**, 80–85.
21 Y. Zhang, J. Zhou, X. Chen, L. Wang and W. Cai, *Chem. Eng. J.*, 2019, **369**, 745–757.
22 J. Peng, E. Wu, N. Wang, X. Quan, M. Sun and Q. Hu, *J. Mol. Liq.*, 2019, **274**, 632–638.
23 R. Abazari, A. R. Mahjoub and J. Shariati, *J. Hazard. Mater.*, 2019, **366**, 439–451.
24 P. Ghosh, Y. J. Colón and R. Q. Snurr, *Chem. Commun.*, 2014, **50**, 11329–11331.
25 J. H. Cavka, S. Jakobsen, U. Olsbye, N. Guillou, C. Lamberti, S. Bordiga and K. P. Lillerud, *J. Am. Chem. Soc.*, 2008, **130**, 13850–13851.
26 S. Rojas, J. A. R. Navarro and P. Horcajada, *Dalt. Trans.*, 2021, 10.1039/d0dt03637d.
27 D. Yang and B. C. Gates, *ACS Catal.*, 2019, **9**, 1779–1798.
28 E. Grabowska, A. Zaleska, S. Sorgues, M. Kunst, A. Etcheberry, C. Colbeau-Justin and H. Remita, *J. Phys. Chem. C*, 2013, **117**, 1955–1962.
29 M. R. DeStefano, T. Islamoglu, S. J. Garibay, J. T. Hupp and O. K. Farha, *Chem. Mater.*, 2017, **29**, 1357–1361.
30 Z. Hasan and S. H. Jhung, *J. Hazard. Mater.*, 2015, **283**, 329–339.
31 Z. Jin, X. Wang, Y. Sun, Y. Ai and X. Wang, *Environ. Sci. Technol.*, 2015, **49**, 9168–9175.
32 I. Ahmed and S. H. Jhung, *Chem. Eng. J.*, 2017, **310**, 197–215.
33 M. C. Bernini, D. Fairen-Jimenez, M. Pasinetti, A. J. Ramirez-Pastor and R. Q. Snurr, *J. Mater. Chem. B*, 2014, **2**, 766–774.
34 S. Rojas, I. Colinet, D. Cunha, T. Hidalgo, F. Salles, C. Serre, N. Guillou and P. Horcajada, *ACS Omega*, 2018, **3**, 2994–3003.
35 B. D. Viezbicke, S. Patel, B. E. Davis and D. P. Birnie, *Phys. status solidi*, 2015, **252**, 1700–1710.
36 J. Li, T. Musho, J. Bright and N. Wu, *J. Electrochem. Soc.*, 2019, **166**, H3029–H3034.
37 M. Brienza, M. Mahdi Ahmed, A. Escande, G. Plantard, L. Scrano, S. Chiron, S. A. Bufo and V. Goetz, *Chemosphere*, 2016, **148**, 473–480.
38 C. Guo, J. Xu, S. Wang, Y. Zhang, Y. He and X. Li, *Catal. Sci. Technol.*, 2013, **3**, 1603–1611.
39 S. Fukahori and T. Fujiwara, *J. Environ. Manage.*, 2015, **157**, 103–110.
40 Y. Ji, Y. Shi, L. Wang, J. Lu, C. Ferronato and J. M. Chovelon, *Sci. Total Environ.*, 2017, **593–594**, 704–712.
41 Cayman, *Safety Data Sheet - Sulfamethazine*, 2017.
42 M. D. Abramoff, P. J. Magalhaes and S. J. Ram, *Biophotonics Int.*, 2004, **11**, 36–43.
43 D. Frenkel and B. Smit, *Understanding Molecular Simulation. From Algorithms to Applications*, 2002.
44 S. Rojas, I. Colinet, D. Cunha, T. Hidalgo, F. Salles, C. Serre, N. Guillou and P. Horcajada, *ACS Omega*, 2018, **3**, 2994–3003.
45 D. Alby, N. El Jeaidi, F. Salles, J. Zajac and C. Charnay, *ACS Appl. Nano Mater.*, 2019, **2**, 497–504.
46 S. J. Ko, T. Yamaguchi, F. Salles and J. M. Oh, *J. Environ. Manage.*, 2021, **277**, 1–11.
47 A. K. Rappé and W. A. Goddard III, *J. Phys. Chem.*, 1991, **95**, 3358–3363.
48 A. K. Rappé, C. J. Casewit, K. S. Colwell, W. A. Goddard III and W. M. Skiff, *J. Am. Chem. Soc.*, 1992, **114**, 10024–10035.